Nanoscale

Accepted Manuscript

This article can be cited before page numbers have been issued, to do this please use: J. G. Tait, M. De Volder, D. Cheyns, P. Heremans and B. Rand, *Nanoscale*, 2015, DOI: 10.1039/C5NR01119A.

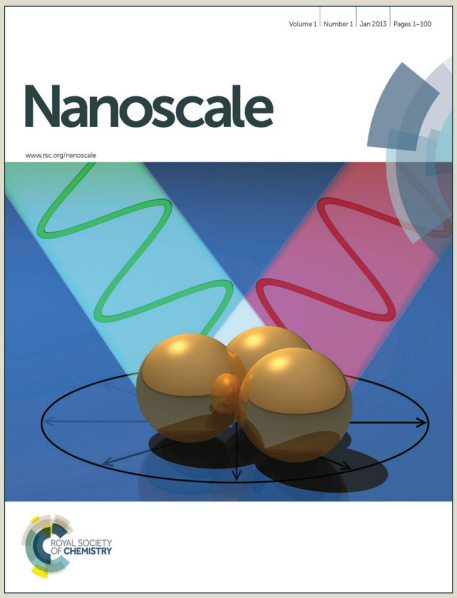

ROYAL SOCIETY OF CHEMISTRY

www.rsc.org/nanoscale

View Article Online
DOI: 10.1039/C5NR01119A

Absorptive Carbon Nanotube Electrodes: Consequences of Optical Interference Loss in Thin Film Solar Cells

Jeffrey G. Tait[a,b], *Michaël De Volder*[c], *David Cheyns*[b], *Paul Heremans*[a,b]*, *Barry P. Rand*[d]*

[a]Dept. of Electrical Engineering, KULeuven, Kasteelpark Arenberg 10, Leuven, B-3001 Belgium

[b] IMEC, Kapeldreef 75, Leuven, B-3001, Belgium

[c]Dept. of Engineering, University of Cambridge, 17 Charles Babbage Road, Cambridge, CB3 0FS, UK

[d]Dept. of Electrical Engineering and Andlinger Center for Energy and the Environment, Princeton University, Princeton, NJ, 08544 USA

* Address correspondence to: *paul.heremans@imec.be*, *brand@princeton.edu*

View Article Online
DOI: 10.1039/C5NR01119A

Table of Contents Entry

Carbon nanotube electrodes for thin film photovoltaics are ultrasonically spray coated, attaining sheet resistances as low as 3.4 Ω □$^{-1}$ without post-deposition treatments. Organic devices achieved similar performance as those with silver electrodes, while optical simulations of other candidate materials elucidate device design parameters.

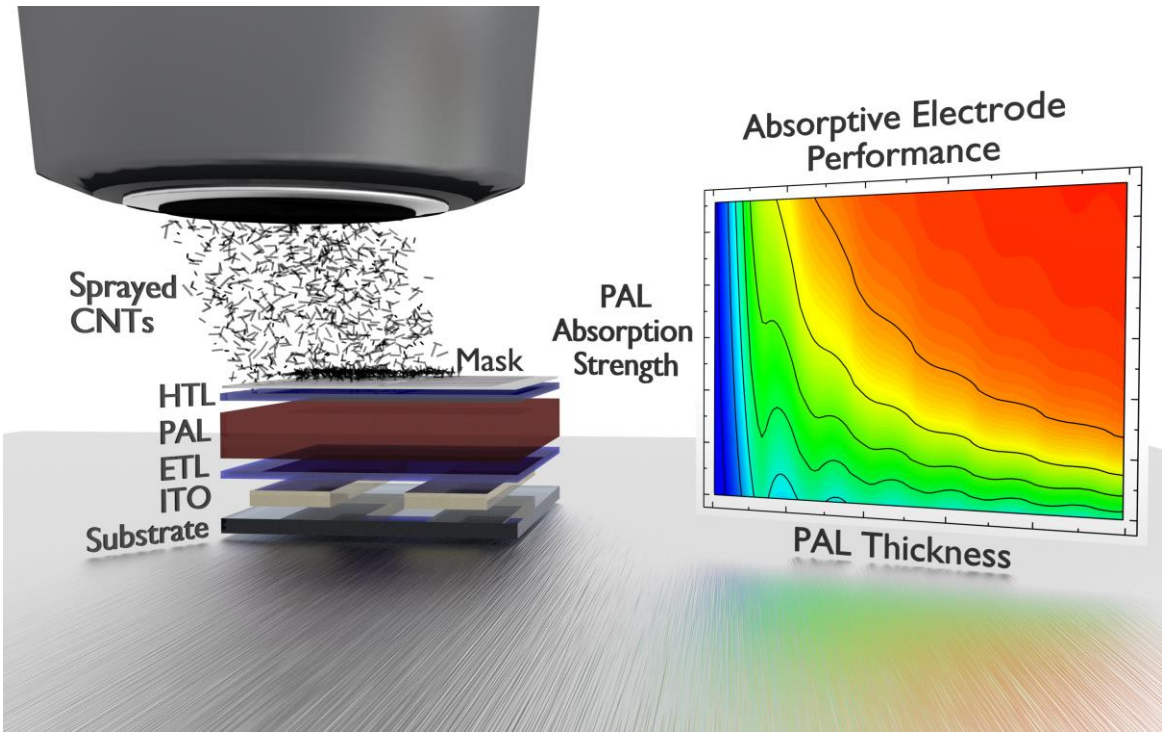

View Article Online
DOI: 10.1039/C5NR01119A

Abstract

A current bottleneck in the thin film photovoltaic field is the fabrication of low cost electrodes. We demonstrate ultrasonically spray coated multiwalled carbon nanotube (CNT) layers as opaque and absorptive metal-free electrodes deposited at low temperatures and free of post-deposition treatment. The electrodes show sheet resistance as low as 3.4 $\Omega\ \square^{-1}$, comparable to evaporated metallic contacts deposited in vacuum. Organic photovoltaic devices were optically simulated, showing comparable photocurrent generation between reflective metal and absorptive CNT electrodes for photoactive layer thickness larger than 600 nm when using archetypal poly(3-hexylthiophene) (P3HT) : (6,6)-phenyl C_{61}-butyric acid methyl ester (PCBM) cells. Fabricated devices clearly show that the absorptive CNT electrodes display comparable performance to solution processed and spray coated Ag nanoparticle devices. Additionally, other candidate absorber materials for thin film photovoltaics were simulated with absorptive contacts, elucidating device design in the absence of optical interference and reflection.

View Article Online
DOI: 10.1039/C5NR01119A

Introduction

The field of photovoltaics (PV) is a major consumer of silver, with its intrinsically large area devices, and is expected to continue its rapid growth as countries move toward greener energy sources.[1–4] Within the field of thin film PV, interest has been rapidly growing in organic (OPV) and perovskite photovoltaic cells, where lab-based devices have reached above 11% and 20% certified efficiencies, and further prompted a drive for roll-to-roll scale deposition techniques.[5,6] Most thin film PV technologies require the photoactive layer stack to be sandwiched between two electrodes, with at least one being semi-transparent. The deposition and patterning of such electrodes are one of the most substantial challenges for industrial roll-to-roll production. Vacuum based deposition techniques offer precise thickness control and high conductivity, while being free of post-deposition treatments, at the expense of cost and complexity for roll-to-roll processing. Solution processed alternatives like metal nanowires and nanoparticles, high conductivity polymers, and carbon nanotubes (CNTs) can be coated at low cost, however, they typically require post-deposition annealing or chemical treatments that are usually incompatible with the underlying layer stack.[7–9] These treatments are typically done to remove surfactants used to disperse the conducting nanoparticles, inhibiting charge transport between conducting components.[5,10–17]

Metals, predominantly silver and copper, have been the materials of choice for not only electrodes in PV devices, but also the vast array of high performance electronic devices and circuitry we use on a daily basis. Unfortunately, the utilization of precious metals like silver has its limitations, due to a rising cost stemming from its limited availability.[4,18,19] Printable and solution processed silver is typically deposited in the form of nanoparticles or nanowires, increasing not only material cost, but also raising the substantiated concern for undesirable

View Article Online
DOI: 10.1039/C5NR01119A

bioactivity.[20,21] A suitable replacement should be conductive, earth-abundant, non-reactive, robust, and stable.

Carbon based electrodes have been gaining in popularity as non-metal electrodes capable of being solution processed, with the added benefit that these materials are sufficiently abundant.[22,23] These electrodes, composed of *e.g.* carbon paste, graphitic nanosheets, carbon nanotubes, or graphene also benefit from being nonreactive and mechanically robust, extending device lifetime, and alleviating processing constraints.[7,24–29] Carbon electrodes based on nanotubes or carbon paste have successfully been implemented in both OPV and perovskite devices, attaining performance approaching that of ITO.[16,17,30–35] A strategy common to these prior reports is to implement these conducting layers as the semi-transparent electrode.[13,25,31,33,36–39] However, the purely absorptive nature of carbon layers limits their transparent electrode performance figure of merit and potential use in thin film PV.[8] In contrast, the benefits of carbon electrodes are still unexplored when implemented as an opaque and absorptive electrode, as we demonstrate here.

Optical interference effects must be accounted for in thin film optoelectronic devices with reflective electrodes, such as silver or aluminum. For maximum functionality, the device layer geometry may be optimized by simulating the internal electrical field distribution, and thus maximizing current generation in thin film PV.[40] In contrast, devices with absorptive electrodes lack the assistance of interference, and hence require thicker photo-active layers (PAL) to reach a similar absorbance. Understanding the relationship between the absorption coefficient and PAL thickness gives insight into the condition for fabrication of high performance devices with absorptive electrodes.

To assess the performance of absorptive, metal-free, and solution processed electrodes for thin film optoelectronic applications, we have evaluated multiwalled CNTs (MWCNTs) as top opaque

View Article Online
DOI: 10.1039/C5NR01119A

electrodes in organic photovoltaic devices. The use of MWCNTs as opposed to single walled CNTs here is significant, as the cost of MWCNTs is orders of magnitude less than that of single walled CNTs.[41] A suspension of dispersed MWCNTs (Electra Colour™ - CNTBlack) was patterned via ultrasonic spray coating through a shadow mask and used as-deposited. This paper presents high conductivity and low sheet resistance MWCNT electrodes for OPV devices with performance comparable to both solution processed and evaporated Ag electrodes. Furthermore, the CNT electrodes are processable on top of the photoactive blend and metal oxide materials. Optical simulations elucidate the need for a long optical path length, *i.e.* a thick PAL or strong absorption coefficient, and a guideline is presented for the implementation of absorptive contacts in thin film photovoltaics, as a function of the material properties.

View Article Online
DOI: 10.1039/C5NR01119A

Materials and Methods

The CNT ink used in these experiments was a MWCNT hydrocarbon suspension (Electra Colour™ - CNTBlack) provided by Owen Research. Patterned glass/ITO substrates were purchased from TFD (3x3 cm^2, $R_S = 20\ \Omega\ \square^{-1}$). All substrates were cleaned in ultrasonic baths of detergent, deionized water, acetone, and 2-propanol. The P3HT 4002-EE was purchased from Rieke Metals, while the [60]PCBM was purchased from Nano-C.

All device fabrication steps were carried out in a N_2 environment. Titania sol-gel in ethanol was spin coated to give 5 nm thick layers. Solutions of P3HT and PCBM in 1,2-ortho-dichlorobenzene (oDCB): 1,3,5-trimethylbenzene were mixed and stirred for at least 8 hours at 80 ˚C prior to deposition. The concurrently pumped spray coating was performed with a Sono-Tek Corp. AccuMist 120 kHz ultrasonic nozzle fixed to an ExactaCoat system. An animation of the CNT spraying process is shown in the supporting information. The top contact of MoO_3 and Ag were thermally evaporated at a pressure of 10^{-7} Torr through a shadow mask to thickness of 10 and 150 nm, respectively, defining devices with an area of 0.13 cm^2.

Atomic force microscope (AFM) images were recorded on a Picoscan PicoSPM LE scanning probe microscope operated in tapping mode. Kelvin probe measurements were carried out with a Veeco Multimode AFM operated in lift mode at a height of 25 nm and temperature of 333 K. A gold coated Si tip (MikroMasch NSC36/Cr-Au) was used. Film thicknesses were measured with a Dektak D150 (Veeco Instruments) surface profilometer. Scanning electron microscope images were captured with a Philips XL30. Sheet resistance was measured with a four point probe on layers sprayed on glass. The current density vs. voltage measurements were done with a Keithley 2602A Source-Measure Unit and an Abet solar simulator producing 100 $mWcm^{-2}$ AM1.5G illumination. External quantum efficiency was measured with coupled and monochromated Xe

View Article Online
DOI: 10.1039/C5NR01119A

and quartz halogen lamps calibrated by a Si photodiode. Reflectivity measurements were measured with the EQE equipment, modified with an integrating sphere, and done through the air/glass/layer interface. Both background and substrate contributions were subtracted from the measured values in the shown figures.

Optical simulations were carried out using transfer matrix optical modeling of the electric field within the device stacks, with layer optical constants measured by ellipsometry (GES5, Sopralab).[40,42] Since the roughness of the CNT layer precludes the measurement of accurate optical constants, the absorptive nature of the CNT layer was approximated with a 1 μm thick MoO_3 layer, accounting for the PAL to transport layer interface. Since the model assumes flat interfaces and no scattering, the thick MoO_3 layer accounts for the rough interface and purely absorptive nature of the CNT layer by approximating a thick absorptive layer and eliminating optical interference contributions from the MoO_3/CNT interface.

View Article Online
DOI: 10.1039/C5NR01119A

Results and Discussion

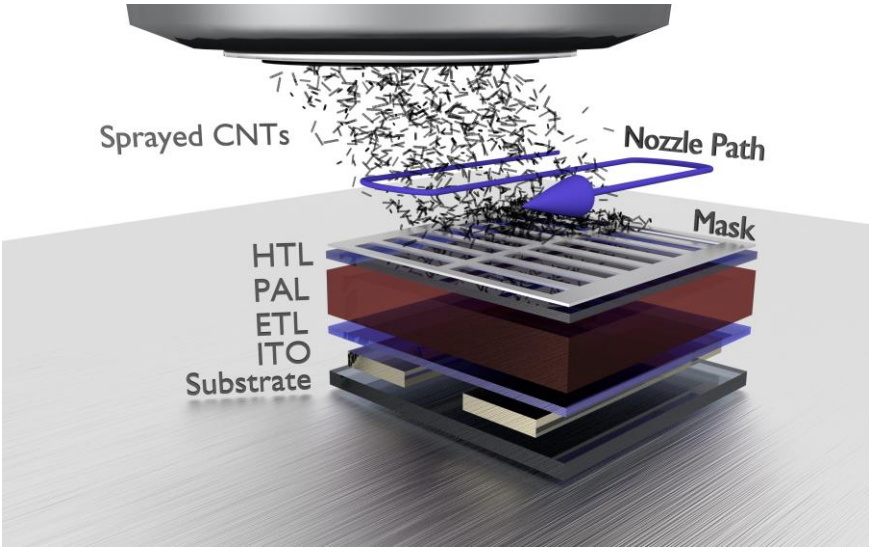

Figure 1. *Schematic representation of multipass spray coating of CNT electrodes through a shadow mask, with the blue arrow showing the overlapping raster pattern. The inverted architecture is comprised of patterned indium tin oxide (ITO) on a glass substrate, followed by the deposition of an electron transport layer (ETL), photoactive layer (PAL), hole transport layer (HTL), and patterned MWCNT electrodes.*

Multiwalled CNT layers were deposited using a multipass raster of the ultrasonic spray coating nozzle, schematically shown in Fig. 1. Due to the low vapor pressure at room temperature of the CNT ink, the substrate was held at an elevated temperature of 70 ˚C during the deposition. This temperature was the lowest temperature necessary to prevent the accumulation of wet droplets upon subsequent passes, and provided well-defined electrode areas through the mask. The facile and controlled accumulation of CNTs into films (scanning electron microscope (SEM) images shown in Fig. 2a,b) provided regulated layer thickness between 50 - 4000 nm. A visibly opaque layer was obtained with a CNT layer thickness above approximately 500 nm.

View Article Online
DOI: 10.1039/C5NR01119A

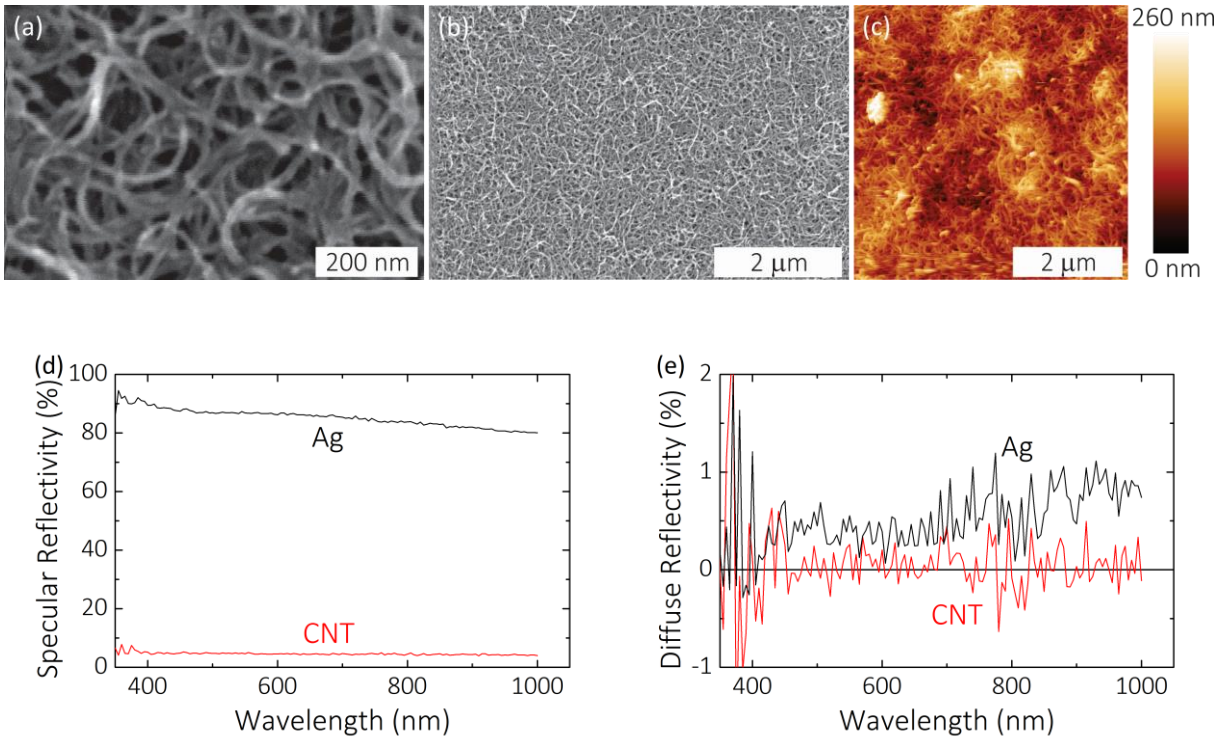

Figure 2. *(a, b) Scanning electron microscope images of 4 µm thick spray coated MWCNT films. (c) Atomic force microscope image of surface topography for a 4 µm thick MWCNT layer. (d) Specular and (e) diffuse reflectivity of a 100 nm thick evaporated Ag and 4 µm thick spray coated MWCNT films, measured through the glass substrate.*

Table 1. *Spray coated CNT, spray coated and sintered Ag nanoparticle (NP), and evaporated Ag layer thickness, sheet resistance as measured with the 4-point probe technique, conductivity, and Kelvin probe measured work function.*

	MWCNT	**Ag NPs**[43]	**Ag (Evap.)**
Thickness (nm)	4000	300	100
Sheet Resistance ($\Omega\ \square^{-1}$)	3.4	1.3	2.4
Conductivity (10^6 S m^{-1})	0.074	2.5	4.2
Work function (eV)	5.4	-	[4.3-4.7]

View Article Online
DOI: 10.1039/C5NR01119A

Spray coated CNT layers of 4 μm thickness showed a measured sheet resistance value of 3.4 Ω □$^{-1}$, comparable to 100 nm thick Ag electrodes with 2.4 Ω □$^{-1}$, indicative of the potential to replace Ag with CNTs. The electrical characterization of the CNT film is summarized in Table 1, along with the work of Girotto, et. al. for spray coated and sintered at 150 °C Ag nanoparticle (NP) layers, and the corresponding data for an evaporated Ag layer.[43,44] The conductivity of these CNT layers was calculated to be 7.4 x 10^4 S m^{-1}. A CNT layer thickness of 4 μm was implemented in this study, because it achieves equal electrical performance to Ag electrodes while increasing the thickness provides diminishing returns for sheet resistance.

The MWCNTs used in this study cost approximately 10 times less than bulk Ag and 600 times less than Ag NP, only considering material cost. The density of these MWCNTs is roughly 10^3 kg m^{-3} and that of bulk Ag is 10^4 kg m^{-3}, leading to an area density of 4 g m^{-2} and 1 g m^{-2}, respectively. We assume the area density of Ag NP electrodes is comparable to bulk Ag for similar performance, since the deposition parameters and sintering conditions strongly impact the packing density. Thus, neglecting the extra cost of vacuum over solution processed deposition, MWCNT electrodes are 2.5 times less than that of bulk silver and 150 times less than Ag NPs. Moreover, the price of Ag is expected to continue its rise, doubling over the past 10 years, while the price of CNTs has dropped by 10 times over the same time span; the price of CNTs is expected to continue decreasing due to economies of scale, reduced cost of feedstock, increased yield, and reduced energy consumption.[41]

Another requirement for the replacement of metal electrodes is the work function alignment of the CNT layer to enable charge extraction from the photoactive layer. A Kelvin probe AFM was used to measure the layer work function. A potential difference of 0.5 eV was measured relative

View Article Online
DOI: 10.1039/C5NR01119A

to a 4.9 eV gold reference,[45] giving a work function of 5.4 eV. This deep work function makes the CNT layer a suitable candidate for the hole extracting anode, and suitable to replace Ag electrodes with a work function between 4.3 and 4.7 eV.[46]

The perfect absorber quality of CNT films is shown with the specular and diffuse reflectivity (Fig. 2d,e) of evaporated Ag and spray coated CNT films, measured though the glass substrate. While Ag demonstrates a high specular reflectivity between 80-90%, CNT films have a minimal specular reflectivity of 5%, this reflectivity may be related to the residual dispersant agent used to suspend CNT in solution. Neither of the films show substantial diffuse components, indicating that neither electrode scatters light and that the CNT film is highly absorptive over the solar-cell relevant spectral range. In the majority of OPV literature, a reflective top metal contact is used, leading to the establishment of optical interference effects, the first two nodes corresponding to photoactive layer (PAL) thicknesses of approximately 90 and 250 nm. As in this work absorptive CNT layers are used, the interference pattern, and thus the optimal PAL thickness, will be different.

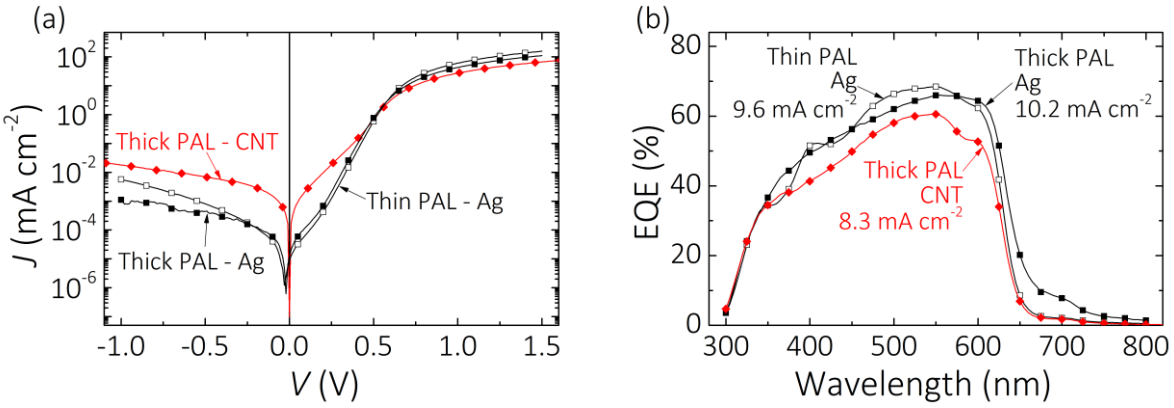

Figure 3. *(a) Dark current density vs. voltage, and (b) external quantum efficiency (EQE) vs. wavelength for both thin (230 nm, open black squares) and thick (600 nm, filled black squares) PAL with Ag electrodes, along with thick PAL (600 nm) with CNT electrodes (red filled diamonds).*

View Article Online
DOI: 10.1039/C5NR01119A

Table 2. *Performance values for best performing P3HT:PCBM devices fabricated with the same equipment and with different top electrodes and PAL thicknesses.*

	PAL Thickness (nm)	**η (%)**	**FF (%)**	**V_{OC} (mV)**	**J_{SC} (mA cm^{-2})**
Conventional	240	4.2	72	620	9.1
Conventional	660	3.7	66	590	9.4
Inverted	230	3.6	62	600	9.6
Inverted	600	2.7	48	560	10.2
Inverted – CNT	600	2.4	51	570	8.3
Inverted – Ag NPs[43]	220	2.5	48	620	8.3

Devices with both conventional architecture, glass/ITO/PEDOT:PSS/P3HT:PCBM/Ca/Ag (anodic ITO), and inverted architecture, glass/ITO/TiO_2/P3HT:PCBM/MoO_3/[Ag or CNT] (cathodic ITO), were fabricated. A photograph of devices fabricated with MWCNT electrodes is shown in Fig. S1. The photoactive layer was deposited via concurrently pumped ultrasonic spray coating as described previously.[44,47] The deep work function of the CNT layers warrants implementation as the top anode in an inverted structure. The dark current density vs. voltage (*J-V*) and external quantum efficiency (EQE) data for a device with a 600 nm thick PAL and CNT top electrode is shown in Fig. 3. The equivalent inverted devices with thick (600 nm) and thin (230 nm) PAL and Ag electrodes are also shown. The EQE for the CNT device is slightly lower at all wavelengths relative to the Ag electrode devices. Notably, the EQE of both thick devices resembles the absorption spectrum of the material, whereas optical interference effects at

View Article Online
DOI: 10.1039/C5NR01119A

wavelengths around 400 nm are noticeable in the thin Ag-based device. Furthermore, the long wavelength absorption near 700 nm benefits from the reflective electrode in the thick Ag-based device, whereas this contribution to EQE is only weakly discernable in the thin Ag and CNT devices. The measured device performance for devices with Ag, Ag NP, and CNT electrodes are listed in Table 2. These devices were fabricated with the same equipment; the conventional and Ag NP data have been published previously.[43,44] The CNT based devices show comparable performance to both evaporated and solution processed Ag electrodes on thick photoactive layers.

View Article Online
DOI: 10.1039/C5NR01119A

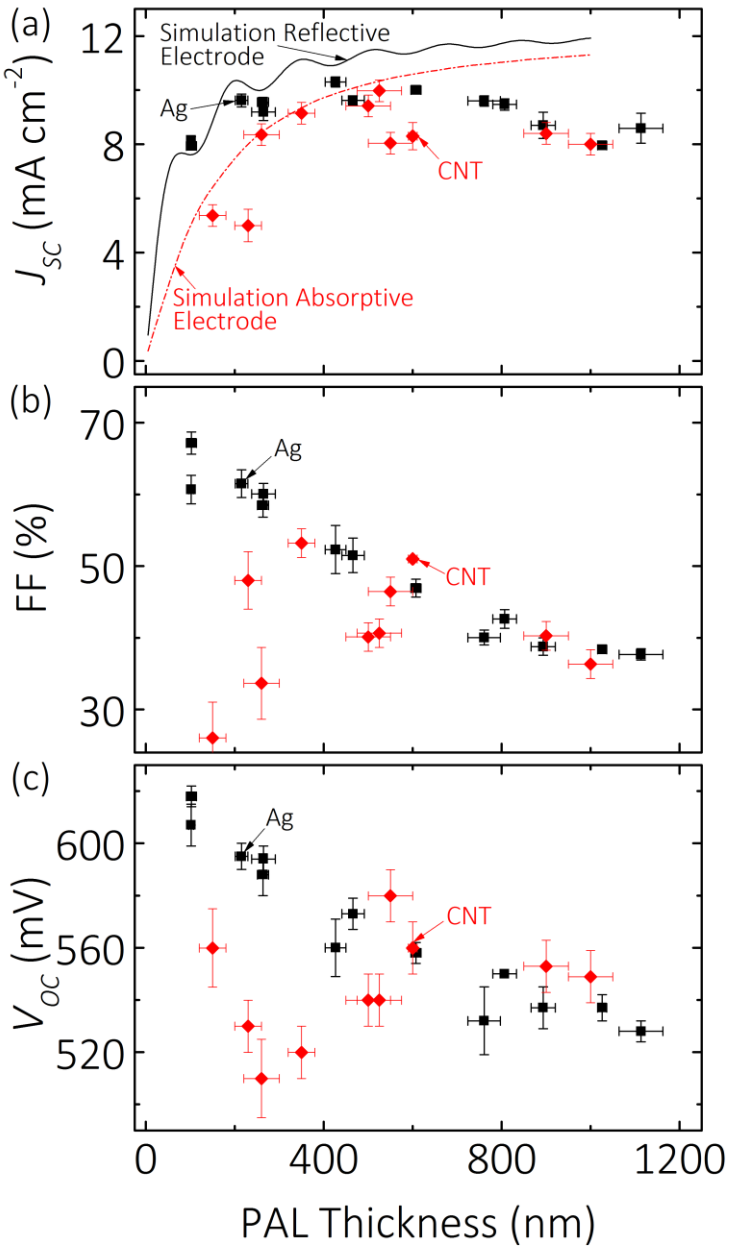

Figure 4. *Plots of (a) short circuit current density (J_{SC}), (b) fill factor (FF), and (c) open circuit voltage (V_{OC}) vs. PAL thickness for measured inverted architecture devices with Ag (black squares) or CNT (red diamonds) electrodes. Error bars account for device-to-device differences in performance and layer thickness over a substrate. Optically simulated J_{SC} values for the reflective (solid black line) or absorptive (dashed red line) electrode devices are shown.*

View Article Online
DOI: 10.1039/C5NR01119A

The photoactive layer thickness was swept between 30 and 1000 nm for inverted architectures with Ag electrodes with the device performance metrics shown in Fig. 4. Devices with 2 and 3 μm thick photoactive layers were also fabricated, shown in Fig. S2; these thicker devices continued the decreasing trend in short circuit current density (J_{SC}) and open circuit voltage (V_{OC}), while fill factor (FF) remained constant at 40%. The drop in J_{SC} for devices thicker than 300 nm is due to a space charge limited current. The imbalance in charge carrier mobilities in the bulk of the photoactive layer causes a build-up of carriers and band bending at the fast-carrier extracting contact.[48] The flat band region near the opposing contact increases bulk charge carrier recombination, decreasing current collection.[49] A decreasing carrier concentration, and thus quasi Fermi-level separation, with increasing PAL thickness explains the drop in V_{OC}. The FF shows an absolute 30% decrease from 100 to 600 nm PAL thickness, substantially more than that reported for conventional architecture devices.[44] A possible explanation for the difference between architectures is a shifted space charge region altering charge extraction.[49–51]

Optical simulations, via transfer matrix optical modeling of the electric field within the device stacks, were carried out as a function of PAL thickness for the inverted device architecture with absorptive and with Ag electrodes. The loss of optical interference effects in thin devices with absorptive electrodes is apparent, relative to the Ag devices.

The measured performance values for devices with absorptive CNT electrodes are shown in Fig. 4. For thin devices, the J_{SC} trend agrees with the optical simulation, and approaches the values of the reflective devices as the thickness increases beyond 500 nm. Regardless of contact material, the space charge limited current reduces J_{SC} for thick devices and limits the useful thickness range for organic photovoltaic devices. Absorptive electrode devices with a thickness less than 300 nm

View Article Online
DOI: 10.1039/C5NR01119A

display low FF and V_{OC}, which is likely due to a decreased tolerance to damage relative to the thicker devices. A reduced electrode deposition rate may lessen this drop.

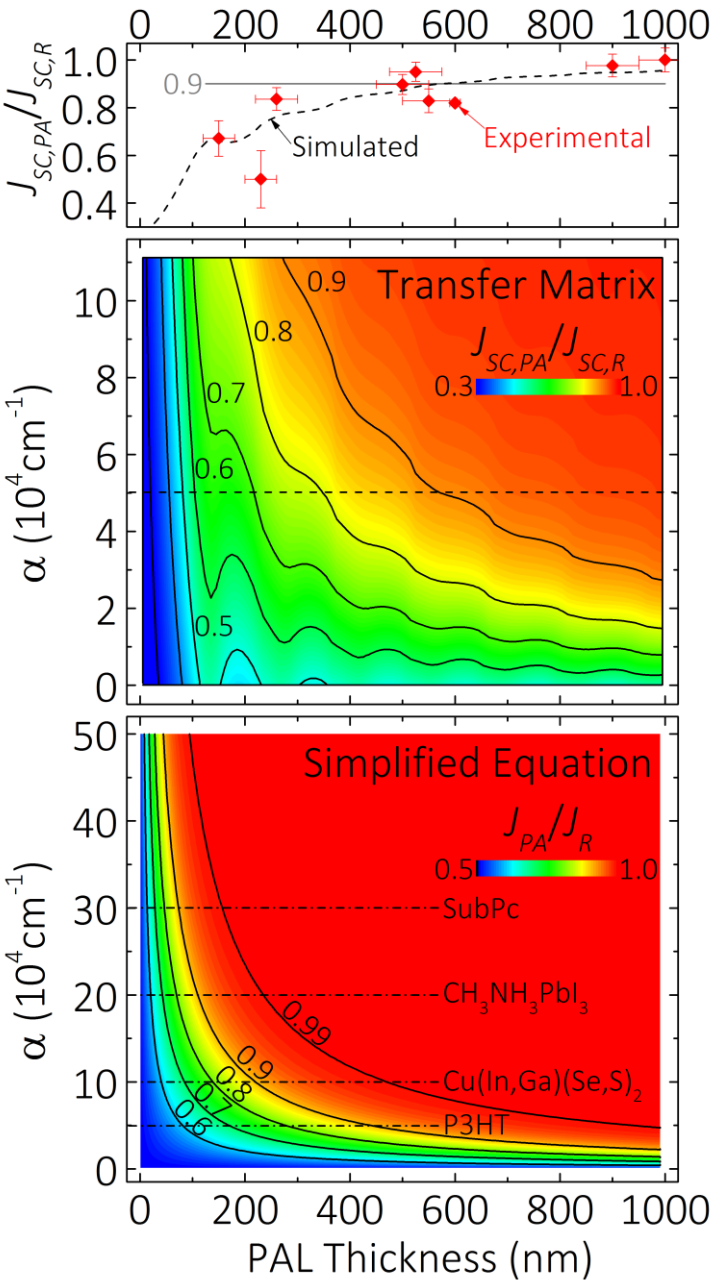

Figure 5. *The upper contour plot shows the J_{SC} ratio between simulated devices with perfect absorber (PA) and with reflective (R) Ag electrodes as a function of thickness and absorption*

View Article Online
DOI: 10.1039/C5NR01119A

coefficient (α) at 563 nm (peak of P3HT:PCBM absorption). The dashed contour line for the measured absorption coefficient of 5x10^4 cm^{-1} of P3HT:PCBM is shown in the upper line plot. The simplified equation, $d(\lambda) = -\frac{1}{\alpha(\lambda)} ln(J_R(\lambda)/J_{PA}(\lambda) - 1)$, is plotted in the lower contour plot with the ratio of photocurrents as a function of PAL thickness and absorption coefficient, where only the absorption at a single wavelength is considered. The approximate peak absorption coefficients for several prominent thin film photovoltaic materials are shown, including: small organic molecule boron subphthalocyanine chloride (SubPc), $CH_3NH_3PbI_3$ perovskite, $Cu(In,Ga)(Se,S)_2$, and P3HT:PCBM.

To investigate the influence of the photoactive material absorption coefficient in devices with absorptive electrodes, devices with reflective Ag and with perfect absorber electrodes were optically simulated, as described in the Materials and Methods section, as a function of PAL thickness and absorption coefficient ($\alpha(\lambda)$). For the latter, the absorption profile of a P3HT:PCBM system is scaled, and the peak absorption at a wavelength of 563 nm is reported, where the value of 5x10^4 cm^{-1} (indicated by a horizontal dashed line in Fig. 5) corresponds with the actual extinction coefficient as measured by ellipsometry. For every PAL thickness and absorption strength, the optimal thickness of an optically transparent spacer layer (with a refractive index of 2 and similar to the hole transporting MoO_3 used in the fabricated devices) between the PAL and anodic contact was calculated to produce the maximum possible J_{SC}. The resulting contour plot of the ratio of J_{SC} for absorptive and reflective contacts is shown in Fig. 5, along with the line plot for the case of the real P3HT:PCBM system. The individual J_{SC} contour plots for each case are shown in Fig. S3. To obtain a 90% J_{SC} ratio value, a layer thickness of 600 nm is required for P3HT:PCBM, while a thickness of only 300 nm is sufficient if the absorption strength could be doubled. The ratio of J_{SC} values for fabricated devices with absorptive CNT electrodes to those

View Article Online
DOI: 10.1039/C5NR01119A

with reflective Ag electrodes is also shown in Fig. 5. The agreement between the simulation and experimental data confirms the predictive capability of the simulations described here.

The maximum photocurrent generation in devices with perfect absorber (PA) electrodes follows the Beer-Lambert law, $J_{PA}(\lambda) = I_0(\lambda)\left(1 - e^{-\alpha(\lambda)d}\right)$, where I_0 is the incident light intensity, λ is wavelength, and d is PAL thickness. The maximum photocurrent generation with a perfect reflector (R) electrode occurs with the peak doubling of the electric field, *i.e.* the peak quadrupling of the absorption. Including the valleys in the interference pattern where the electrical field can drop to zero, a mean doubling of the absorption enhancement can be expected, *viz* $J_R(\lambda) = I_0(\lambda)\left(1 - e^{-2\alpha(\lambda)d}\right)$. The PAL thickness required to attain a certain ratio of maximum possible current densities is $d(\lambda) = -\frac{1}{\alpha(\lambda)} ln\left(J_R(\lambda)/J_{PA}(\lambda) - 1\right)$. Note that this simplified equation differs from the optical simulations shown in Fig. 5, because the equation is only valid at a single specified absorption coefficient; an integration over all wavelengths is required to calculate the real J_{sc} ratio. According to the above formula a P3HT:PCBM device attains a photocurrent ratio of 90% with a PAL thickness of 440 nm and α(563 nm)=5x10^4 cm^{-1}, while a PAL thickness of 550 nm is required for α(420 nm)=4x10^4 cm^{-1}. The equation has been implemented with other thin film photovoltaic materials to attain 90% current ratio between absorptive and reflective electrodes. Perovskite based materials (*e.g.* $CH_3NH_3PbI_3$), with α(470 nm)=2x10^5 cm^{-1} as peak absorption, require a minimal PAL thickness of 110 nm according to the equation. An optical simulation, taking the full wavelength spectrum into account and with the plots shown in Fig. S4, shows that a planar perovskite device with a perfect absorber electrode requires only 250 nm to attain 90% of the possible photocurrent; while a 1000 nm thick PAL produces 97% photocurrent relative to a reflective electrode. Evaporated small molecules can exhibit even higher extinction coefficients. As an example, boron subphthalocyanine chloride (SubPc), used in energy cascade devices, has a

View Article Online
DOI: 10.1039/C5NR01119A

peak absorption coefficient of $3x10^5$ cm^{-1} and requires a 73 nm PAL thickness.[52] Another thin-film technology, $Cu(In,Ga)(Se,S)_2$, shows an absorption coefficient near 10^5 cm^{-1}, and requires a minimum of a 220 nm thick PAL.[53] The simplified equation is shown in the bottom panel of Fig. 5, with labels for the specified materials; a plot of the required PAL thickness for a specified absorption coefficient and photocurrent ratio is shown in Fig. S5.

Conclusions

In conclusion, this work shows the implementation of ultrasonic spray coating for the deposition of absorptive and opaque multiwalled carbon nanotube electrodes that are free of metals and post deposition treatments. The as-deposited 4 μm thick multiwalled CNT layers reached sheet resistance as low as 3.4 $\Omega\,\square^{-1}$ and conductivity of 7.4 x 10^4 S m^{-1}. The CNT electrode was constrained to function as the anode in this work, with its measured work function of 5.5 eV. Inverted architecture devices with absorptive CNT electrodes showed equal performance to both evaporated and spray coated Ag electrodes, given thick photoactive layers. Optical simulations of the complete device stack showed that current density with an absorptive CNT electrode can be comparable to a reflective Ag electrode by merely increasing the optical path length; a layer thickness of at least 600 nm was required for the archetypal P3HT:PCBM system. Furthermore, this work provides design recommendations aimed toward photoactive materials with higher absorption coefficients, permitting thinner films and decreasing the reliance on expensive and reflective electrodes. Overall the treatment-free opaque MWCNT electrode via ultrasonic spray coating presents itself as a cost-effective and scalable solution processed alternative to evaporated metal electrodes.

View Article Online
DOI: 10.1039/C5NR01119A

Supporting Information

The supporting information includes an animation of the MWCNT spray coating process, and five figures, including: a photograph of completed devices with MWCNT electrodes, performance metrics for devices with photoactive layer thickness up to 3000 nm, contour plots of simulated devices used to build Fig. 5, simulation data for perovskite devices, and a contour plot of the simplified equation of photoactive layer thickness required to attain a specified photocurrent ratio (x-axis) and absorption coefficient (y-axis).

Author Contributions

J.G. Tait carried out the experiments and wrote the manuscript. M. De Volder synthesized the CNT ink with Owen Research. D. Cheyns and P. Heremans were scientific advisors. B.P. Rand was the principle investigator. All authors reviewed and contributed to the manuscript.

Acknowledgements

This research has received partial funding from the Flemish Government – Department of Economics, Science and Innovation. J.G. Tait acknowledges partial funding from the Natural Sciences and Engineering Research Canada. M. De Volder acknowledges partial funding from the ERC Starting Grant 337739. The authors gratefully acknowledge the preliminary work on absorptive carbon-based electrodes by Dr. E. Meshot, the deposition of perovskite layers for optical data by W. Qui, and the fruitful discussions on the optical properties of thin films with Dr. U.W. Paetzold. Kelvin probe measurements were done by Dr. S. Van Reenen at the Technische Universiteit Eindhoven.

The authors declare no competing financial interests.

View Article Online
DOI: 10.1039/C5NR01119A

References

1 N. Espinosa, R. García-Valverde, A. Urbina and F. C. Krebs, *Sol. Energy Mater. Sol. Cells*, 2011, **95**, 1293–1302.

2 N. Espinosa, F. O. Lenzmann, S. Ryley, D. Angmo, M. Hösel, R. R. Søndergaard, D. Huss, S. Dafinger, S. Gritsch, J. M. Kroon, M. Jørgensen and F. C. Krebs, *J. Mater. Chem. A*, 2013, **1**, 7037–7049.

3 A. de La Tour, M. Glachant and Y. Ménière, *Energy*, 2013, **62**, 341–348.

4 C. F. Yu, W. G. J. H. M. van Sark and E. A. Alsema, *Renew. Sustain. Energy Rev.*, 2011, **15**, 324–337.

5 S. Ye, A. R. Rathmell, Z. Chen, I. E. Stewart and B. J. Wiley, *Adv. Mater.*, 2014, **26**, 6670–6687.

6 M. A. Green, K. Emery, Y. Hishikawa, W. Warta and E. D. Dunlop, *Prog. Photovoltaics Res. Appl.*, 2015, **23**, 1–9.

7 S. Park, M. Vosgueritchian and Z. Bao, *Nanoscale*, 2013, **5**, 1727–1752.

8 J. G. Tait, B. J. Worfolk, S. A. Maloney, T. C. Hauger, A. L. Elias, J. M. Buriak and K. D. Harris, *Sol. Energy Mater. Sol. Cells*, 2013, **110**, 98–106.

9 Y. H. Kim, C. Sachse, M. L. Machala, C. May, L. Müller-Meskamp and K. Leo, *Adv. Funct. Mater.*, 2011, **21**, 1076–1081.

10 J. Krantz, T. Stubhan, M. Richter, S. Spallek, I. Litzov, G. J. Matt, E. Spiecker and C. J. Brabec, *Adv. Funct. Mater.*, 2013, **23**, 1711–1717.

11 L. Hu, H. S. Kim, J.-Y. Lee, P. Peumans and Y. Cui, *ACS Nano*, 2010, **4**, 2955–2963.

12 E. C. Garnett, W. Cai, J. J. Cha, F. Mahmood, S. T. Connor, M. Greyson Christoforo, Y. Cui, M. D. McGehee and M. L. Brongersma, *Nat. Mater.*, 2012, **11**, 241–249.

13 M. W. Rowell, M. A. Topinka, M. D. McGehee, H.-J. Prall, G. Dennler, N. S. Sariciftci, L. Hu and G. Gruner, *Appl. Phys. Lett.*, 2006, **88**, 233506.

14 B. E. Hardin, W. Gaynor, I.-K. Ding, S.-B. Rim, P. Peumans and M. D. McGehee, *Org. Electron.*, 2011, **12**, 875–879.

15 A. J. Stapleton, R. A. Afre, A. V Ellis, J. G. Shapter, G. G. Andersson, J. S. Quinton and D. A. Lewis, *Sci. Technol. Adv. Mater.*, 2013, **14**, 035004.

View Article Online
DOI: 10.1039/C5NR01119A

16 R. a. Hatton, N. P. Blanchard, L. W. Tan, G. Latini, F. Cacialli and S. R. P. Silva, *Org. Electron. physics, Mater. Appl.*, 2009, **10**, 388–395.

17 V. Sgobba and D. M. Guldi, *J. Mater. Chem.*, 2008, **18**, 153.

18 European Commission, *Report on Critical Raw Materials for the EU*, Brussels, 2014.

19 M. Hoffert, K. Caldeira, A. Jain and E. Haites, *Nature*, 1998, **395**, 881–884.

20 X. Chen and H. J. Schluesener, *Toxicol. Lett.*, 2008, **176**, 1–12.

21 S. A. Blaser, M. Scheringer, M. Macleod and K. Hungerbühler, *Sci. Total Environ.*, 2008, **390**, 396–409.

22 S. Stankovich, D. A. Dikin, G. H. B. Dommett, K. M. Kohlhaas, E. J. Zimney, E. A. Stach, R. D. Piner, S. T. Nguyen and R. S. Ruoff, *Nature*, 2006, **442**, 282–286.

23 A. K. Geim and K. S. Novoselov, *Nat. Mater.*, 2007, **6**, 183–191.

24 B. Arash, Q. Wang and V. K. Varadan, *Sci. Rep.*, 2014, **4**, 6479.

25 M. P. Ramuz, M. Vosgueritchian, P. Wei, C. Wang, Y. Gao, Y. Wu, Y. Chen and Z. Bao, *ACS Nano*, 2012, **6**, 10384–10395.

26 M. Majumder, C. Rendall, M. Li, N. Behabtu, J. A. Eukel, R. H. Hauge, H. K. Schmidt and M. Pasquali, *Chem. Eng. Sci.*, 2010, **65**, 2000–2008.

27 L. Hu, D. S. Hecht and G. Grüner, *Chem. Rev.*, 2010, **110**, 5790–5844.

28 Y. Zemen, S. C. Schulz, H. Trommler, S. T. Buschhorn, W. Bauhofer and K. Schulte, *Sol. Energy Mater. Sol. Cells*, 2013, **109**, 155–159.

29 S. Y. Kim, J. Hong, R. Kavian, S. W. Lee, M. N. Hyder, Y. Shao-Horn and P. T. Hammond, *Energy Environ. Sci.*, 2013, **6**, 888.

30 F. Zhang, X. Yang, H. Wang, M. Cheng, J. Zhao and L. Sun, *ACS Appl. Mater. Interfaces*, 2014, **6**, 16140–16146.

31 R. C. Tenent, T. M. Barnes, J. D. Bergeson, A. J. Ferguson, B. To, L. M. Gedvilas, M. J. Heben and J. L. Blackburn, *Adv. Mater.*, 2009, **21**, 3210–3216.

32 T. M. Barnes, J. D. Bergeson, R. C. Tenent, B. A. Larsen, G. Teeter, K. M. Jones, J. L. Blackburn and J. van de Lagemaat, *Appl. Phys. Lett.*, 2010, **96**, 243309.

33 S. Kim, J. Yim, X. Wang, D. D. C. Bradley, S. Lee and J. C. DeMello, *Adv. Funct. Mater.*, 2010, **20**, 2310–2316.

View Article Online
DOI: 10.1039/C5NR01119A

34 S. N. Habisreutinger, T. Leijtens, G. E. Eperon, S. D. Stranks, R. J. Nicholas and H. J. Snaith, *Nano Lett.*, 2014, **14**, 5561–5568.

35 C.-Y. Su, A.-Y. Lu, Y.-L. Chen, C.-Y. Wei, P.-C. Wang and C.-H. Tsai, *J. Mater. Chem.*, 2010, 20, 7034.

36 Z. Wu, Z. Chen, X. Du, J. M. Logan, J. Sippel, M. Nikolou, K. Kamaras, J. R. Reynolds, D. B. Tanner, A. F. Hebard and A. G. Rinzler, *Science (80-.).*, 2004, **305**, 1273–1276.

37 A. Du Pasquier, H. E. Unalan, A. Kanwal, S. Miller and M. Chhowalla, *Appl. Phys. Lett.*, 2005, **87**, 203511.

38 X. Li, F. Gittleson, M. Carmo, R. C. Sekol and A. D. Taylor, *ACS Nano*, 2012, **6**, 1347–1356.

39 S.-I. Na, Y.-J. Noh, S.-Y. Son, T.-W. Kim, S.-S. Kim, S. Lee and H.-I. Joh, *Appl. Phys. Lett.*, 2013, **102**, 043304.

40 L. A. A. Pettersson, L. S. Roman and O. Inganäs, *J. Appl. Phys.*, 1999, **86**, 487.

41 M. F. L. De Volder, S. H. Tawfick, R. H. Baughman and A. J. Hart, *Science*, 2013, **339**, 535–539.

42 H. Gommans, D. Cheyns, T. Aernouts, C. Girotto, J. Poortmans and P. Heremans, *Adv. Funct. Mater.*, 2007, **17**, 2653–2658.

43 C. Girotto, B. P. Rand, S. Steudel, J. Genoe and P. Heremans, *Org. Electron.*, 2009, **10**, 735–740.

44 J. G. Tait, B. P. Rand and P. Heremans, *Org. Electron.*, 2013, **14**, 1002–1008.

45 R. Fowler, *Phys. Rev.*, 1931, **38**, 45–56.

46 A. W. Dweydari and C. H. B. Mee, *Phys. Status Solidi*, 1975, **27**, 223–230.

47 J. G. Tait, C. Wong, D. Cheyns, M. Turbiez, B. P. Rand and P. Heremans, *IEEE J. Photovoltaics*, 2014, **4**, 1538–1544.

48 P. W. M. Blom, V. D. Mihailetchi, L. J. A. Koster and D. E. Markov, *Adv. Mater.*, 2007, **19**, 1551–1566.

49 G. F. A. Dibb, M.-A. Muth, T. Kirchartz, S. Engmann, H. Hoppe, G. Gobsch, M. Thelakkat, N. Blouin, S. Tierney, M. Carrasco-Orozco, J. R. Durrant and J. Nelson, *Sci. Rep.*, 2013, **3**, 3335.

50 V. Mihailetchi, J. Wildeman and P. W. M. Blom, *Phys. Rev. Lett.*, 2005, **94**, 126602.

View Article Online
DOI: 10.1039/C5NR01119A

51 T. Kirchartz, T. Agostinelli, M. Campoy-Quiles, W. Gong and J. Nelson, *J. Phys. Chem. Lett.*, 2012, **3**, 3470–3475.

52 K. Cnops, B. P. Rand, D. Cheyns, B. Verreet, M. A. Empl and P. Heremans, *Nat. Commun.*, 2014, **5**, 3406.

53 S. Theodoropoulou, D. Papadimitriou, K. Anestou, C. Cobet and N. Esser, *Semicond. Sci. Technol.*, 2009, **24**, 015014.